

Shear velocity estimates on the inner shelf off Grays Harbor, Washington, USA

Christopher R. Sherwood^{a,*}, Jessica R. Lacy^b, George Voulgaris^c

^aUS Geological Survey, Coastal and Marine Geology, 384 Woods Hole Road, Woods Hole, MA 02543-1598, USA

^bUS Geological Survey, Santa Cruz, CA, USA

^cUniversity of South Carolina, Columbia, SC, USA

Received in revised form 17 March 2006

Available online 25 September 2006

Abstract

Shear velocity was estimated from current measurements near the bottom off Grays Harbor, Washington between May 4 and June 6, 2001 under mostly wave-dominated conditions. A downward-looking pulse-coherent acoustic Doppler profiler (PCADP) and two acoustic-Doppler velocimeters (field version; ADVFs) were deployed on a tripod at 9-m water depth. Measurements from these instruments were used to estimate shear velocity with (1) a modified eddy-correlation (EC) technique, (2) the log-profile (LP) method, and (3) a dissipation-rate method. Although values produced by the three methods agreed reasonably well (within their broad ranges of uncertainty), there were important systematic differences. Estimates from the EC method were generally lowest, followed by those from the inertial-dissipation method. The LP method produced the highest values and the greatest scatter. We show that these results are consistent with boundary-layer theory when sediment-induced stratification is present. The EC method provides the most fundamental estimate of kinematic stress near the bottom, and stratification causes the LP method to overestimate bottom stress. These results remind us that the methods are not equivalent and that comparison among sites and with models should be made carefully.

© 2006 Elsevier Ltd. All rights reserved.

Keywords: Inner shelf; Bottom stress; Turbulence; Sediment-induced stratification; Sediment transport; Sediment resuspension

1. Introduction

Shear velocity u_* is a critical parameter for sediment transport and mixing in the bottom boundary layer. Shear velocity is defined as $u_* = \sqrt{\tau_b / \rho_0}$, where ρ_0 is the average fluid density and τ_b is the bottom shear stress exerted on the flow

by skin friction and form drag. In situ estimates of u_* are critical for sediment-transport calculations and for testing models. Practical and theoretical considerations make it difficult to determine u_* in shelf and nearshore environments, and a simple but robust measurement technique would be invaluable. New instruments and methods have been developed for estimating u_* from measurements. In particular, high-resolution acoustic profilers and the eddy-correlation (EC) technique proposed by Trowbridge (1998) are promising advances. Some of the methods discussed here have fared well in estuarine and shelf environments, where mean currents

*Corresponding author. Tel.: +1 508 457 2269;

fax: +1 508 457 2310.

E-mail addresses: csherwood@usgs.gov (C.R. Sherwood),

jlacy@usgs.gov (J.R. Lacy), gvoulgaris@geol.sc.edu

(G. Voulgaris).

dominate over waves, but the greatest difficulties lie in wave-dominated environments. The purpose of this paper is to evaluate the practical application of three methodologies for estimating shear velocity in challenging environments like the inner shelf. We review methods for estimating shear velocity from field measurements (Section 2) and provide examples from our Grays Harbor data (Section 3). These data reveal systematic differences in u_* estimates among the methods and we discuss the interpretation (Section 4) and implications of these differences (Section 5).

2. Methods for estimating shear velocity u_*

Three methods that have been used to estimate shear velocity from flow measurements are the EC method, the log-profile (LP) method, and the inertial-dissipation (ID) method (Huntley, 1988). Advances in instrumentation and analysis methods have improved these methods since Huntley's (1988) paper. Here, we briefly review the theory, analyses, and practical considerations associated with each method.

2.1. EC method

The EC method relies on direct estimates of the horizontal components of turbulent shear stresses τ_{zx} and τ_{zy} (also called Reynolds stresses) associated with time-averaged correlation in turbulent velocity fluctuations:

$$\begin{aligned}\tau_{zx}/\rho_0 &= -\overline{u'w'}, \\ \tau_{zy}/\rho_0 &= -\overline{v'w'},\end{aligned}\quad (1)$$

where overbars represent time averaging, and primes denote the turbulent part of horizontal (u , v) and vertical (w) velocity components comprised of the sum of Reynolds-averaged, wave-associated, and turbulent components (e.g., $u = \bar{u} + \tilde{u} + u'$).

Estimates of Reynolds stresses based on measurements are very sensitive to small changes in the orientation of the current meter, and can also be biased by gentle bottom slopes and weak reflected waves (Grant and Madsen, 1986; Trowbridge, 1998). However, Trowbridge (1998) proposed a method for reducing wave-induced bias in Reynolds stress estimates by using two measurements of velocity at locations separated by a distance much smaller than the organized motions of waves and mean circulation, but greater than the correlation

length scale of turbulent motions which scale with elevation above the bed in the bottom boundary layer. The estimate of $\overline{u'w'}$ is

$$\overline{u'w'} \approx \frac{1}{2}\text{cov}(\Delta u, \Delta w) = \frac{1}{2}\overline{\Delta u' \Delta w'} + \frac{1}{2}\overline{\Delta \tilde{u} \Delta \tilde{w}}, \quad (2)$$

where u and w are now the measured velocity components in the sensor coordinate system (which may be imperfectly aligned with real coordinate system by rotation about each axis by a small angle) and the Δ operator denotes the difference between quantities measured at the two measurement locations. There is a corresponding equation for $\overline{v'w'}$. The first term on the right-hand side of Eq. (2) is the turbulence component comprised of the average turbulent stress (for the two locations) and turbulence bias associated with sensor misalignment and turbulence correlations among the two sensors. Trowbridge (1998) argues that the turbulence bias is small as long as the sensor misalignment is of order 10^{-2} , the sensor separation is 1–2 times their height above the bottom, and the sensor separation is larger than the excursion amplitude of the wave-induced motion. The second term is the wave bias, which Trowbridge (1998) argues is an order of magnitude smaller than typical near-bottom Reynolds stresses as long as the distance between the sensors is much smaller than the length scale for variations in \tilde{u} and \tilde{v} .

The EC method provides a direct estimate of the Reynolds stress, averaged spatially between the sensors. In the constant stress layer, Reynolds stress is (by definition) closely related to bottom stress (e.g., Heathershaw and Simpson, 1978), so estimates of u_* in unidirectional flow can be formed as

$$-\overline{u'w'}/u_*^2 = 1 - \frac{1}{R}, \quad (3)$$

where the Reynolds number $R = \kappa u_* z / \nu$ and ν is the kinematic viscosity of water (Tennekes and Lumley, 1972; Kim et al., 2000). In fully turbulent flow, $R \gg 1$, so $u_*^2 \approx -\overline{u'w'}$. The primary advantage of the EC method, as modified by Trowbridge (1998), is that it requires high-frequency, three-axis velocity measurements at only two locations, and several suitable instruments are commercially available. Voulgaris et al. (1997) and Shaw and Trowbridge (2001) report success with this technique in continental shelf environments with surface waves.

2.2. LP method

The LP method relies on theoretical (e.g., Tennekes and Lumley, 1972) and empirical observations

that shear in the bottom boundary layer is determined by a characteristic shear velocity u_* and height above the bottom z , as

$$\partial|U|/\partial z = u_*/(\kappa z), \quad (4)$$

where $|U|$ is mean speed and $\kappa = 0.408 \pm 0.004$ is the von Kármán constant (Long et al., 1993). The region near the bed where this expression is valid is called the log layer (e.g., Grant and Madsen, 1986; Cacchione and Drake, 1990). Integration of Eq. (4) yields the log profile

$$|U| = (u_*\kappa)\ln(z/z_0), \quad (5)$$

where z_0 is the hydraulic roughness length. Application of the LP method requires measurements of mean velocity at several elevations in the log layer (at least two, commonly three or four, preferably more). After rewriting Eq. (5) as

$$|U| = (u_*/\kappa)\ln(z) - (u_*/\kappa)\ln(z_0), \quad (6)$$

it is clear that u_* and z_0 can be estimated from a linear least-squares fit, where $|U|$ is the dependent variable, $\ln(z)$ is the independent variable, u_*/κ is the slope, and $-(u_*/\kappa)\ln(z_0)$ is the intercept.

Inferences of u_* from all of the techniques discussed here assume that the flow is steady, turbulent, unstratified, and horizontally uniform with a well-developed boundary layer thick enough to profile. One advantage of the LP method is that the profiles themselves can be tested for log-linearity. Gross et al. (1992) point out, however, that log-linear profiles are only expected in a statistical sense, so individual deviations from the ideal profile may or may not indicate that the fundamental assumptions have been violated.

The primary practical consideration of the LP method is the need to measure at several points, possibly with intrusive (flow-disturbing) sensors. The statistical power of this technique improves with the number of elevations used, but when mechanical, electromagnetic, acoustic travel-time, or single-point acoustic Doppler current meters are used, the size of the sampling volumes and the need to minimize flow disturbance generally limits the number of elevations to 4–6, at least in shelf and estuarine bottom boundary layer flows. Acoustic Doppler profiling current meters are less intrusive and generally afford measurements at more elevations, but with some instruments (including the one we used for this study), there is a trade-off between the number of elevation bins and measurement uncertainty. In addition, there are few commercially

available instruments that promise the spatial resolution, velocity range, and sampling speed required to profile the bottom boundary layer in wave-dominated environments. Cheng et al. (1999) have shown that an RD Instruments, Inc. 1200-kHz broadband acoustic Doppler profiler, operating in mode 5, can produce detailed profiles in fast tidal currents with small waves, but to our knowledge, the Grays Harbor experiment is the first attempt to measure velocity profiles in a wave-dominated bottom boundary layer with a downward-looking PCADP.

2.3. ID method

The ID method (also known as the spectral-dissipation method) makes use of the theoretical relationship between spectral amplitude of turbulent kinetic energy in the inertial range and dissipation rate ε . The ID method for use in the atmospheric boundary layer was first described by Deacon (1959) and is reviewed by Champagne et al. (1977). Development and application of the technique in the marine boundary layers can be traced through the papers of Bowden (1962), Gross and Nowell (1983), Grant et al. (1984), Huntley (1988), Huntley and Hazen (1988), Agrawal et al. (1992), Green, (1992), Gross et al. (1994), Xu et al. (1994), and Trowbridge and Elgar (2001).

The ID method offers the promise of single-point estimates of shear velocity, but estimates of dissipation rate from velocity measurements are difficult. According to Kolomogorov's hypothesis, turbulent motions are generated at large length scales l_p , controlled by the dimensions of the flow, and the inertia of these motions produces a cascade of eddies with ever-decreasing length scales until viscous forces become important and the energy is dissipated into heat. In a boundary layer, the length scale of the eddies in which turbulence is produced is proportional to the distance from the boundary ($l_p \sim z$) and the length scale for dissipation l_d is order $(\nu^3/\varepsilon)^{1/4}$, where ν is the kinematic molecular viscosity, about $1.35 \times 10^{-6} \text{ m}^2 \text{ s}^{-1}$. When the scale of production is much greater than the dissipation length scale ($l_p \gg l_d$), an inertial subrange exists where the three-dimensional spectrum of turbulent motions $E(k)$ is scaled by the dissipation rate and decreases with three-dimensional wavenumber k at the characteristic $-5/3$ slope, according to

$$E(k) = a\varepsilon^{2/3}k^{-5/3}, \quad (7)$$

where a is the three-dimensional Kolmogorov constant. Eq. (7) provides the basis for estimating dissipation rate from wavenumber spectra. Researchers, however, typically record velocity fluctuations over time at a fixed location and rely on Taylor's (1938) "frozen turbulence" hypothesis to infer wavenumber spectra from frequency spectra. The frozen turbulence assumption is a valid approximation in unidirectional flows if the time scale for rotation of a turbulent eddy t_t is much longer than the drift time scale t_d . The drift time scale can be estimated as $t_d = (ku_d)^{-1}$ for an eddy with length scale $1/k$ to be advected past a measurement point with mean drift velocity u_d . The rotational time scale for the eddy is $t_t = \varepsilon^{-1/3} k^{-2/3} = l^{1/3} k^{-2/3} u_t^{-1}$, where the dissipation rate scales with the turbulence velocity scale u_t and length scale l as $\varepsilon = u_t^3/l$. Thus, the criteria for using the frozen turbulence hypothesis is

$$(kl)^{1/3} \gg \frac{u_t}{u_d}. \quad (8)$$

Surface waves complicate application of the frozen turbulence hypothesis by introducing an oscillatory motion with a time scale between t_t and t_d . Lumley and Terray (1983) showed that advection of the turbulence by wave motions elevated spectral energy densities at frequencies greater than the wave frequency, even for purely monochromatic wave motion. Gross et al. (1994) extended the approach of Lumley and Terray (1983) to account for wave-induced increases in velocity spectra measured near the bed and compared the resulting shear velocity estimates with those obtained using the LP method. They found that the results agreed within the (rather large) combined uncertainty of the two methods. Most recently, Bryan et al. (2003) described methods for estimating dissipation rates based on idealized linear wave motions.

Trowbridge and Elgar (2001) developed model velocity spectra for the inertial subrange (at frequencies significantly higher than the wave frequency) under combined waves and currents, specialized for unidirectional waves with horizontal orbits (i.e., near-bottom conditions). Their model for horizontal spectra (E_{uu} , E_{vv}) is

$$E_{uu}(\omega) + E_{vv}(\omega) = \frac{21}{55} \alpha \varepsilon^{2/3} |U|^{2/3} \omega^{-5/3} I\left(\frac{\sigma}{|U|}, \theta\right) + \text{constant noise level} \quad (9)$$

and for vertical spectra E_{ww} is

$$E_{ww}(\omega) = \frac{12}{55} \alpha \varepsilon^{2/3} |U|^{2/3} \omega^{-5/3} I\left(\frac{\sigma}{|U|}, \theta\right), \quad (10)$$

where the function I is

$$I\left(\frac{\sigma}{|U|}, \theta\right) = \frac{1}{\sqrt{2\pi}} \left(\frac{\sigma}{|U|}\right)^{2/3} \int_{-\infty}^{\infty} \left[x^2 - 2\left(\frac{|U|}{\sigma}\right) \cos(\theta)x + \left(\frac{|U|}{\sigma}\right)^2 \right]^{1/3} \exp\left(-\frac{1}{2}x^2\right) dx \quad (11)$$

and where the spectra are defined such that their integral over all ω equals the variance of the time series, $\omega = 2\pi f$ is angular frequency, f is frequency in Hz, $|U|$ is the mean current speed over a burst interval much longer than the wave period, σ^2 is the variance of the wave-induced horizontal velocity, $\alpha \approx 1.5$ is the empirical Kolmogorov constant, θ is the angle between the mean current and the unidirectional wave oscillations, and x is a dummy variable for integration (Trowbridge and Elgar, 2001, their Eqs. (6,7, and A13)).

Estimates of shear velocity from dissipation-rate measurements assume that there is a local balance between dissipation and shear production of turbulence, as

$$\varepsilon = -\overline{u'w'} \frac{\partial u}{\partial z} - \overline{v'w'} \frac{\partial v}{\partial z}. \quad (12)$$

(This discussion is derived mostly from Tennekes and Lumley (1972) but follows more closely the notation of Huntley, 1988; Green, 1992; Gross et al., 1994.) This is consistent with the law of the wall and with the constant stress assumptions, and provides the basis for estimating u_* from measurements of ε at elevation z :

$$u_*^3 = \varepsilon k z. \quad (13)$$

The primary advantage of the ID method is that, under optimal conditions, it requires point measurements at only one elevation above the bottom. The principal drawbacks to practical application in the field are (1) the difficulty in separating turbulence from wave motions, measurement noise, and wakes shed by instrumentation and (2) ensuring that the Reynolds number is high enough and that the measurements are above the critical elevation so that there is clear spectral separation between scales of production and the Kolmogorov scale.

Various approaches to the first problem have been tried but, as Gross et al. (1994) point out, the

technique has not lived up to its promise. Huntley (1988) has provided a correction for conditions where the Reynolds number is low (or the measurements are too close to the bed).

3. Data set

The data discussed here were obtained with instruments mounted on a tripod located on the 9-m isobath on the northern flank of the ebb-tidal delta formed at the entrance to Grays Harbor, Washington at a location designated MIA on the site map (Fig. 1). The adjacent North Beach is a gently sloping dissipative beach comprised of well-sorted fine gray sand with mixed lithology typical of the relatively immature sediment of the Columbia River littoral cell. Sediment at the tripod location is well-sorted fine sand (mean size = 0.13 mm) with a median settling velocity of 9 mm/s (Table 1). Wave energy is high, especially in winter, when significant wave heights have reached 8 m at the Coastal Data Information Center (CDIP) buoy moored at 40-m depth off Grays Harbor (Fig. 1).

Instruments were mounted on a tripod 2.5 m high with 4.2-cm diameter legs (Fig. 2; Table 2). Instrument cases and battery packs were mounted at least 1.65 m above the bottom (mab). Velocity data were obtained with a pulse-coherent acoustic-Doppler profiler (PCADP) and

Table 1

Summary of bottom sediment properties based on grab samples at Site MIA and analyses by settling tube

Size (mm)	Size (ϕ)	Weight percent	Settling velocity (mm/s)
0.25	2 and coarser	2	>28
0.21	2.25	4	21
0.18	2.5	10	16
0.15	2.75	26	12
0.13	3	53	9
0.11	3.25	3	6
0.09	3.5 and finer	2	<4

Grain sizes were estimated from laboratory settling velocities by inverting the Gibbs et al. (1971) equation, which was also used to estimate in situ settling velocities for temperature of 10 °C and salinity of 30 PSU (Landerman et al., 2004).

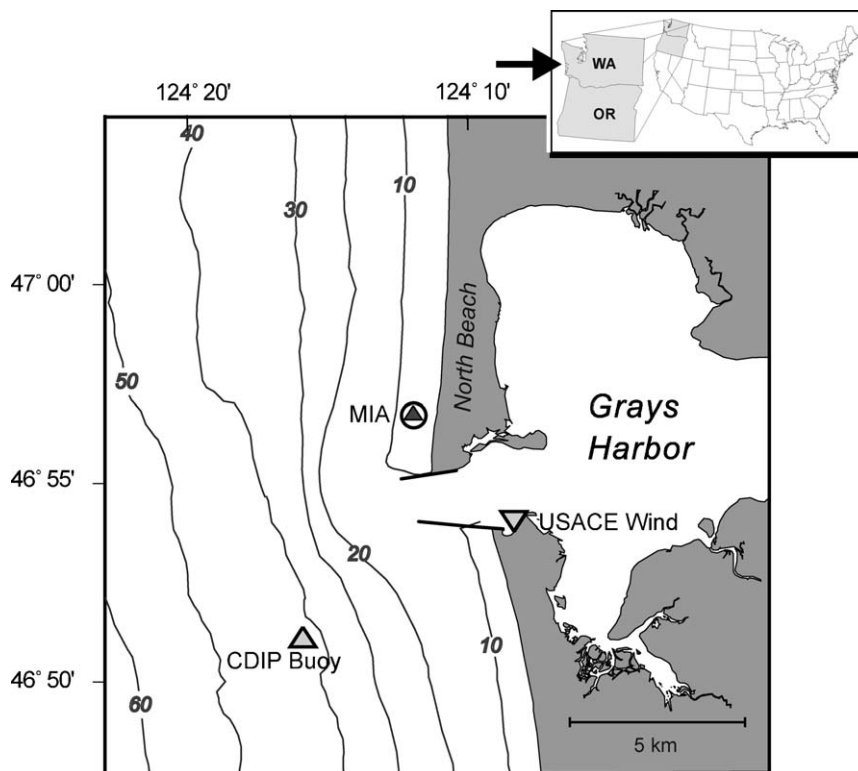


Fig. 1. Map of the study area on the inner shelf off Grays Harbor, Washington. Locations of the deployment site (designated MIA), Coastal Data Information Program (CDIP) Grays Harbor wave buoy (no. 03601, depth = 40 m), and US Army Corps of Engineers (USACE) wind instrument are indicated.

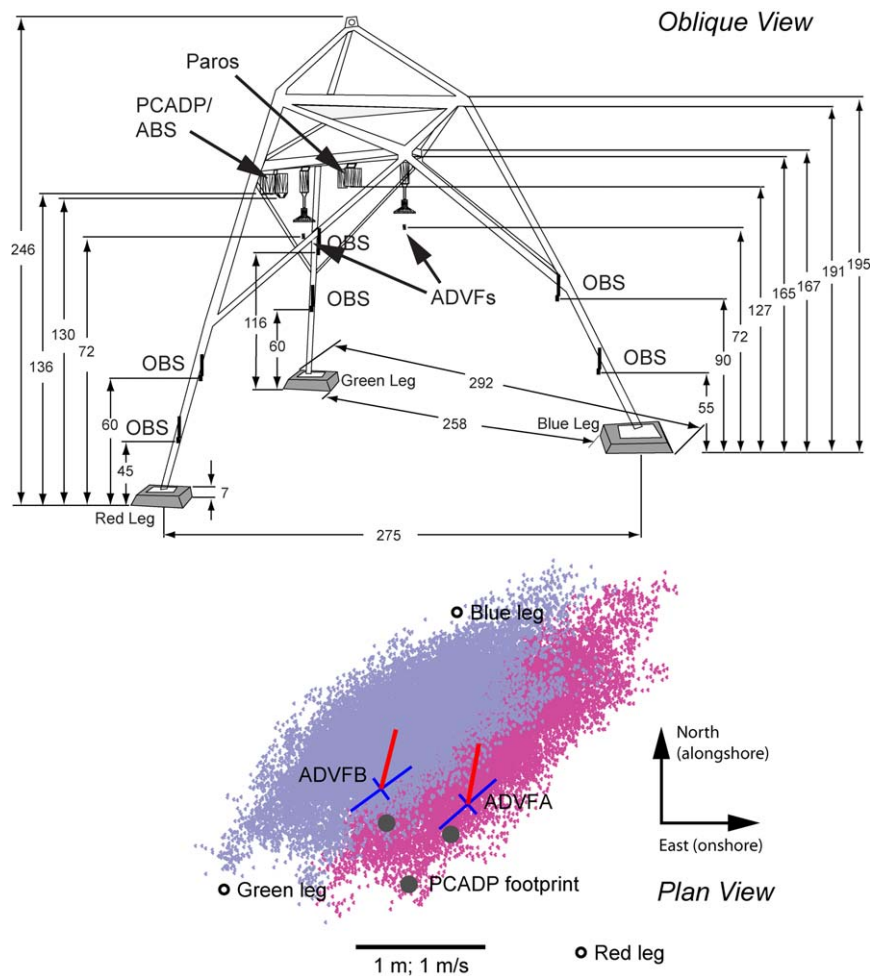


Fig. 2. Schematic drawing of tripod deployed at MIA (upper panel; see also Table 2). Dimensions are in cm and elevations are nominal (i.e., measured from flat bottom before tripod settling). Plan view of instrument sampling locations (lower panel). Relative locations of ADVF A and B (center of blue crosses) and the bottom footprint of PCADP beams (solid black circles) are shown. Tripod legs are open black circles. Light red and blue dots form a scatter plot of current velocity from ADVF A and B, respectively; blue crosses indicate principal components of velocity; and red lines indicate mean velocity. Data shown are for large waves from the SW with strong northward flow.

Table 2
Summary of instruments, measurement elevations, and sampling schemes

Instrument	Nominal measurement elevations	Sampling rates	Comments
Sontek pulse-coherent acoustic Doppler profiler (PCADP)	0.94–0.08 mab 8 bins 0.11-m bin size	20 min at 1 Hz every hour	Also measured pressure and range to the bottom
Two Sontek acoustic Doppler velocimeters, field model (ADVFs)	0.72	20 min at 20 Hz every 2 h	Synchronized, ~0.8 m horizontal separation
Aquatec acoustic backscatter sensor (ABS) 278-017	1.36–0.21 mab 128 bins 0.09-m bin size	30 min at 64 Hz, averaged to 1 Hz every hour	Three frequencies (1, 2.5 and 5 MHz)
Six D&A optical backscatter sensors (OBS)	0.45, 0.55, 0.6, 0.6, 0.9, and 1.16 mab	4 for 20 min at 20 Hz every 2 h 2 for 20 min at 1 Hz every hour	Two logged by each ADVF, 2 logged by PCADP

two acoustic-Doppler velocimeters (field version; ADVFs). The PCADP recorded velocity profiles, distance to the bottom along each of its three beams, and pressure (Table 2). The two ADVFs (designated A and B) were synchronized and sampled three components of velocity at two points separated by 0.8 m (horizontally in the cross-shore direction) at 0.3–0.5 mab. Instrument elevation varied as the tripod feet scoured into the bottom and bed topography changed; the actual elevation for each burst was obtained from the PCADP data. Cross-correlations of ADVF burst data confirm that the data are synchronous; in more than 99% of the cases, maximum correlation occurs at zero lag. Six optical backscatter sensors (OBSs) were mounted on the tripod at various elevations and an acoustic backscatter sensor (ABS) provided profiles related to suspended-sediment concentrations (Fig. 2; Table 2). Results from this experiment have been published by Lacy and Sherwood (2004) and Lacy et al. (2005). Additional information and the data are available in a USGS Data Series report (Landerma et al., 2004).

Water depth at the MIA tripod location averaged 9 m, and ranged from 7.1 to 10.6 m during the study period, which was 1500 UT May 4–1400 UT June 5, 2001. Average significant wave height at the buoy was 1.7 m and peaked at 4.2 m (Fig. 3(c)). Upwelling-favorable winds from the NW prevailed most of the time and wave heights were less than 2 m and approached generally from the west ($\sim 277^\circ$). On four occasions (May 4–5, May 14, May 15, and May 28) wind direction shifted to the SW, wave heights increased to 2.5–4 m, and waves approached from the SW. The interval May 20–24 was a period with low waves and upwelling-favorable wind with diurnal fluctuations. Current directions at ~ 0.5 mab during the study were oriented alongshore: the principal axis of the hourly velocities, which explained 90% of the variance, was aligned toward $358^\circ/178^\circ$. Except during the strongest southwesterly storm on May 14–15, the low-frequency alongshore flow at MIA was generally southward (toward 186°) with a vector mean of 0.05 m/s. Periods of strong southward flow were accompanied by near-bottom onshore flows and decreases in water temperature, indicating upwelling (Fig. 3(g) and (h)).

3.1. Data preparation

PCADP data were recorded in beam coordinates, processed to remove velocity ambiguities, and then

rotated into geographic coordinates according to burst-mean heading and tilt measurements from the PCADP compass (Lacy and Sherwood, 2004). ADVF data were recorded in instrument coordinates that were converted from beam coordinates in situ by Sontek firmware. These were rotated to geographic coordinates using the tripod orientation of 190° T (determined with an accuracy of about $\pm 10^\circ$) from ADVF A. We calculated the principal components of horizontal velocity for each burst (essentially a measure of wave direction) and found an offset of 2.3° (median difference over 384 bursts) between the two ADVFs, which we assume was caused by misalignment of the sensors during installation on the tripod. After rotating data from ADVF B by this amount, the final differences in orientation of principal axes had a range of -5.6 to $+2.2^\circ$, with 90% of the bursts in the range -2 to $+0.9^\circ$.

Data from each 20-min burst from the ADVFs were processed to identify and replace apparently spurious data. This was a subjective process, but visual inspection of the data and trials with various methods indicated that the residual difference of instantaneous samples from the low-pass filtered time series provided an effective criterion for defining outliers. Raw burst data were detrended and then smoothed using a low-pass filter with a cutoff-frequency equal to $f_s/6$, where f_s is the sampling frequency (20 Hz). Sampled values that differed by more than 2.8 standard deviations from the smoothed time series were replaced by quadratic or linear interpolation using at least two of seven points on either side of the flagged data. Only the horizontal velocity components were tested, but if either was flagged, data in all three components were replaced by interpolation. On average, about 400 of the 24,000 points were replaced, and usually about 10 points in each burst were identified that could not be replaced because surrounding points were also flagged. These were left unchanged. The mean of each velocity component of data processed in this manner was usually changed by less than 1%, and the variance was usually changed by less than 2%. Results presented in this paper are not qualitatively affected by this process.

We relied on manufacturer calibrations and firmware to convert pressure and temperature measurements to engineering units. Optical backscatter data were converted to estimates of mass concentration using laboratory calibrations with surficial sediment from the site (Landerma et al., 2004).

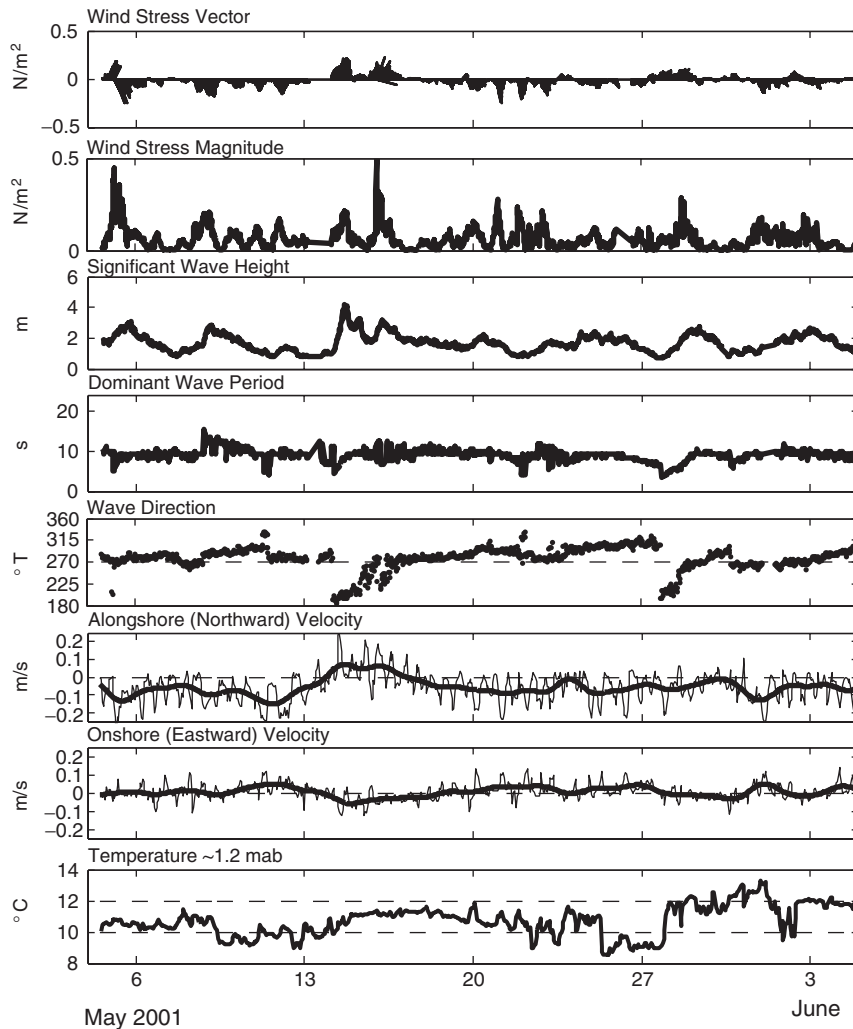


Fig. 3. Time series of winds, waves, currents, and water temperatures during the study period. Wind stress was calculated according to Large and Pond (1981) from USACE wind measurements. Wind vectors indicate direction towards which wind is blowing (oceanographic convention). Wave conditions were measured at the CDIP buoy and currents were measured hourly at ~ 0.7 mab by the PCADP at site MIA. 40-hr low-pass filtered currents are shown with thicker lines in panels (f) and (g).

The ABS data presented problems because the gains were set too high (both a range-variable gain and a fixed gain were used). This meant that the ABS electronics were often saturated by returns, especially those from near the bed during times of high suspended-sediment concentrations, and especially for the 1- and 2.5-MHz signals. The high gain settings also prevented good laboratory calibrations because the saturation problem was exacerbated in our calibration facilities, where the ABS signal was confined and ambient sound levels may have been higher. Thus, the ABS observations presented here are uncalibrated. They are burst-mean profiles normalized by an empirical response profile that,

for each frequency, is the binwise median profile for the entire deployment (a procedure suggested by P. Traykovski, personal communication). The ABS data can only be used to make qualitative inferences about relative changes in suspended-sediment concentrations.

Instrument elevations were determined using their fixed positions on the tripod and the elevation of the PCADP transducer. Slant-range distances from the PCADP transducer to the bed were measured by each of the three beams and, using heading and tilt information, were converted to transducer elevations by instrument firmware. The three elevation estimates are accurate within about 0.01 m but

often differed because of ripples and larger-scale topography beneath the tripod (Lacy et al., 2005). The median value for each burst was used as the elevation of the PCADP transducer. The maximum difference among the three beams (Δr) varied among bursts from 0 to 0.09 m, with a median value of 0.02 m.

3.2. EC method

Burst time series of velocity differences Δu , Δv , and Δw were formed from velocity components measured at the two ADVs (denoted with subscripts A and B), e.g. $\Delta u = u_A - u_B$. Three different estimates of horizontal Reynolds stresses (suggested

by Shaw and Trowbridge, 2001) can be computed from these time series. For example, $\overline{u'w'}$ can be calculated as $\frac{1}{2}\text{cov}(\Delta u, \Delta w)$, $\text{cov}(\Delta u, w_A)$, or $\text{cov}(\Delta u, w_B)$; and there are corresponding estimates for $\overline{v'w'}$. In this paper, we present results using only the first method because it is least likely to be affected by wave bias (Trowbridge, 1998; Shaw and Trowbridge, 2001). The efficacy of velocity differencing for removing wave motions is illustrated in Fig. 4(a) and (c). Shear velocity estimates were calculated as the vector sum of the two components, as

$$u_{*EC} = \left[\left(\frac{1}{2}\text{cov}(\Delta u, \Delta w) \right)^2 + \left(\frac{1}{2}\text{cov}(\Delta v, \Delta w) \right)^2 \right]^{1/4}. \quad (14)$$

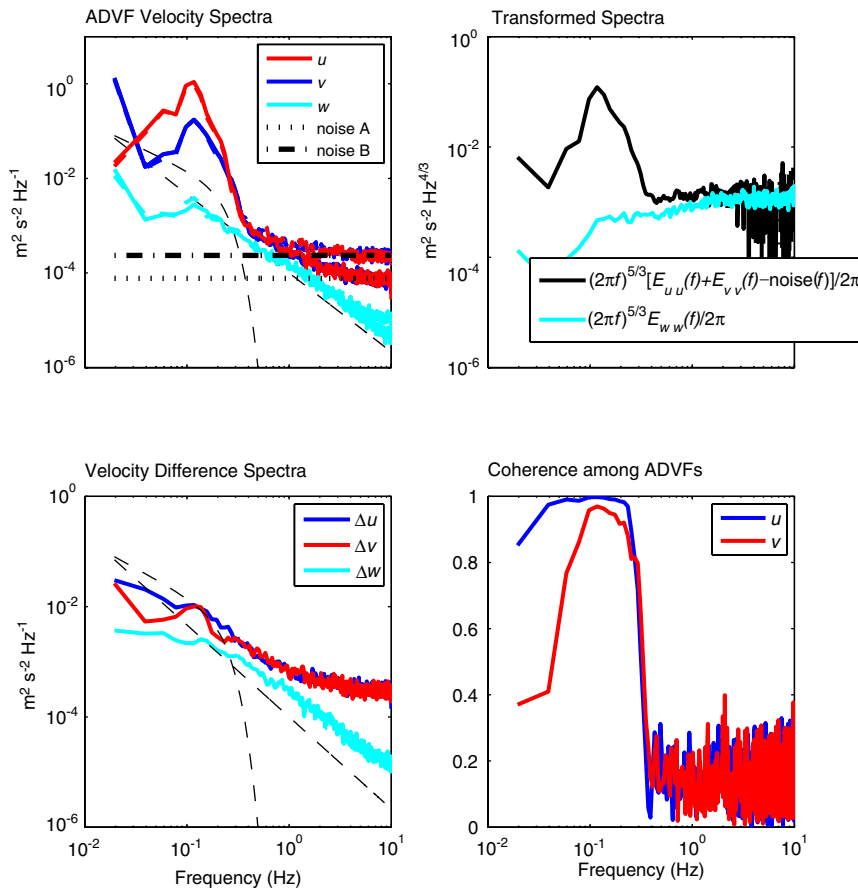


Fig. 4. Velocity spectra from the two ADVs for a representative burst. (a) Autospectral density for the three velocity components (u , v , and w are blue, red, and cyan, respectively; ADFV A is solid, ADFV B is dashed). Also shown are $-5/3$ slope and expected spectra for linear surface-wave motions for depth = 9 m (dashed lines). Dashed and dash-dot lines indicate noise estimates for each ADFV. (b) Transformed spectra for horizontal (black) and vertical (cyan) components for ADFV A. (c) Autospectra for Δu , Δv , and Δw ; same color scheme as (a). (d) Coherence of horizontal components u and v among ADVs (blue and red, respectively). Noise was apparent in u and v components, but not in the w component. Differencing removed most, but not all, of the wave signal. Transformed spectra were typically flat in the inertial subrange (1–2.5 Hz).

We estimated the standard error of covariance estimates as

$$e_{uw}^2 = \frac{1}{N} \left[1 + \frac{C_{uu}C_{ww}}{C_{uw}^2} \right], \quad (15)$$

where C_{uu} , C_{ww} are autocovariances of Δu and Δw , C_{uw} is covariance of Δu with Δw , and N is the degrees of freedom, equal to the number of statistically independent realizations of the turbulence field (Soulsby, 1980; Bendat and Piersol, 1986, p. 273). We estimated N as

$$N = \frac{|U|T}{l} = \frac{|U|n}{zf_s}, \quad (16)$$

where T is the sampling time and is equal to n/f_s , where n is the number of samples ($\sim 24,000$) and f_s is the sampling frequency (20 Hz), l is the turbulence length scale, which scales with z , the measurement elevation (~ 0.35 m), and $|U|$ is burst-mean speed. For typical velocities ranging from 0.05 to 0.5 m/s, this results in N ranging from ~ 170 to ~ 1700 . The median value of N in our data set was 254. We also used the method of Lueck and Wolk (1999) to determine whether our covariance estimates were significantly different than the noise in our data by comparing covariance at lag zero against the distribution of cross covariance at lags longer than the decorrelation time scale $l/|U|$. Most (78%) of the estimates fell into the top or bottom 5% of the probability distribution, suggesting they are significant at the 90% confidence level.

3.3. LP method

Estimates of friction velocity u_{*LP} and apparent hydraulic roughness z_{0a} were calculated by least-squares fits of the PCADP profiles using burst-mean speed as the dependent variable and elevations of the bin centers as the independent variable (Eq. (6)). Fits included data from the four lowest bins that were more than 1.5 bins above the bottom, so bin centers typically ranged from 0.19 to 0.43 mab. We assigned a range of uncertainties to the resulting estimates of u_{*LP} by performing additional fits with elevations for each burst shifted according to the maximum and minimum transducer elevations and adding (or subtracting) the uncertainties associated with the least-squares fits, which were based on the 90% confidence intervals for estimates of the slope and intercept.

3.4. ID method

Spectral estimates of turbulence energy were computed for each of the three velocity components measured by the two ADVFs using the Welch method with a boxcar window. Spectral densities (units of $\text{m}^2\text{s}^{-2}\text{Hz}^{-1}$) were computed, normalized such that the integral over spectrum for each segment matched the variance of the segment. Segments were 4096 points long (204.8 s) and overlapped by 50%. The resulting spectra contained 2048 points at frequencies ranging from ~ 0.005 Hz to the Nyquist frequency (10 Hz), with approximately 9 degrees of freedom (Fig. 4). Spectra from the two ADVFs were highly coherent at frequencies below about 0.4 Hz, where mean flow and wave motions dominated (Fig. 4(d)). Higher-frequency spectra (above 0.4 Hz) of vertical velocities decayed with nearly $-5/3$ slope, but spectra of horizontal components tended to flatten starting around 2 Hz (Fig. 4(a)), suggesting instrument noise. Noise estimates for the horizontal components for each ADVF were calculated as $\text{mean}(E_{uu}(f)) + \text{mean}(E_{vv}(f))$ for $f > 5$ Hz (Trowbridge and Elgar, 2001). The Trowbridge and Elgar (2001) model indicates that dissipation should scale as $\omega^{5/3}E_{ww}(\omega) = (2\pi)^{4/3}f^{5/3}E_{ww}(f)/2\pi$, so the spectra have been transformed accordingly in Fig. 4(b) and median values of $\omega^{5/3}E_{ww}(\omega)$ and $\omega^{5/3}[E_{uu}(\omega) + E_{vv}(\omega) + \text{noise}]$ were calculated over the range 1–2.5 Hz ($2-5\pi\omega$) for each ADVF. The transformed spectra in this range were typically flat (Fig. 4(b)), as intended by the Trowbridge and Elgar (2001) technique. Dissipation rates ε were estimated according to that model (Eqs. (9–11)) using burst-mean speed and standard deviation of velocity along the principal component at each ADVF for $|U|$ and σ , respectively. This procedure resulted in four dissipation-rate estimates for each burst, which we denote as ε_{Auv} , ε_{Aww} , ε_{Buv} , and ε_{Bww} . The four estimates agree closely, but because ADVF A had generally less noise, and because there is less scatter in estimates from the vertical spectra, we use ε_{Aww} for comparison with other methods. Uncertainty in the estimates of ε , denoted as δ_ε , is determined by how well the inertial range is resolved, and cannot be easily estimated (Shaw et al., 2001). We used the range between the 16th- and 84th-percentile values of averaged spectra in the inertial subrange. Estimates of shear velocity u_{*ID} were computed from ε_{Aww} using Eq. (13).

Huntley (1988) and Green (1992) have suggested that these u_{*ID} values should be increased according to

$$u_{*IDC} = [u_{*ID}^3 R_c v / \kappa z]^{1/4}, \quad z < z_c, \quad (17)$$

where critical Reynolds number R_c is taken as 3000, for measurement elevations z less than the critical elevation z_c required for a fully developed inertial subrange. This would increase our estimates by about 20% at unadjusted shear velocities of ~ 0.01 m/s, about 10% at ~ 0.015 m/s, and would have little or no effect on unadjusted shear velocities greater than about 0.02 m/s. We do not include this adjustment in the values of u_{*ID} presented here.

3.5. Model estimates

We have used a one-dimensional (vertical) model of stress, velocity, and sediment-concentration profiles to help interpret the observations. The model (Wiberg and Smith, 1983; Mclean, 1992; Wiberg et al., 1994; Traykovski et al., 2005) assumes a continuous eddy-viscosity profile scaled by wave-induced stresses near the bed and by wave-averaged total bottom stress in the overlying current boundary layer. It requires as input measured mean current velocities \bar{u} and \bar{v} at reference elevation z_r , representative wave-orbital velocity u_{br} , representative wave period T_r , wave direction θ , and information about the bed material (Table 3). The model calculates bottom roughness, including the combined effects of sediment size, ripple geometry (Wiberg and Harris, 1994), and sediment transport (Wiberg and Rubin, 1989). The model iterates to a steady state where profiles of velocity, eddy viscosity, Reynolds stress, suspended-sediment concentration and sediment diffusivity are consistent with the specified flow conditions, total bed stress, and maximum wave-induced stresses that dominate sediment resuspension. Effects of sediment-induced

stratification are included: when sediment is in suspension, parameterization of the buoyancy flux acts to reduce the eddy viscosity, which in turn affects the Reynold stresses.

Our main goal in using the model here is to elucidate the differences among our various estimates of shear velocity. In the model, the average bed stress (and therefore u_{*c}) can be explicitly defined and quantified ($u_{*c} \equiv \sqrt{\tau_b / \rho_0}$), and the model output can be sampled to provide values analogous to field estimates of u_{*LP} (by fitting a log profile to the modeled velocity profile) and $u_{*\tau}$ (defined as $u_{*\tau}^2 \equiv |\tau| / \rho_0 = K_m \partial|U| / \partial z$, where τ is local stress, K_m is the eddy viscosity adjusted for sediment-induced stratification, and $\partial|U| / \partial z$ is the shear), all taken at a specific elevation in the model profile (here, 0.35 mab). A more complicated model (e.g., a two-equation turbulence model) would be needed to estimate u_{*ID} from the modeled dissipation rate.

4. Results

4.1. Overview

The mean speeds and wave-orbital velocities agreed closely among the PCADP (bin 5) and the two ADVFs (for details, refer to Lacy et al., 2005). References to mean speed $|U|$ and representative wave-orbital velocity u_{br} (calculated according to Madsen, 1994) apply equally well to all instruments and are referenced to an elevation that varied over the deployment from 0.3 to 0.46 m, with a median value of 0.35 m. A range of conditions were measured but, in general, mean current speeds were low when compared with wave-orbital velocities. Median current speed was 0.13 m/s, and maximum speed was 0.48 m/s, whereas median wave-orbital velocities were 0.45 m/s and ranged from 0.13 to 0.93 m/s. The maximum ratio of significant wave height to water depth H_s/h was about 0.3, less than the value of ~ 0.7 required for breaking (Komar, 1998), so waves were probably never breaking over the tripod due to shoaling. However, the fine sand beneath the tripod was probably mobile during the entire experiment (based on calculated Shields parameters; Lacy et al., 2005). On average, the ratio of mean speed to wave-orbital velocity was 0.36, and it never exceeded 1.2, so the results presented here represent mostly wave-dominated conditions.

Table 3
Summary of bottom sediment properties used in the model

Nominal size (ϕ)	Weight percent	Critical shear stress (Pa)	Settling velocity (mm/s)
2.5	42	0.18	23
3	53	0.13	8
3.5	3	0.11	4
4	2	0.9	2

A total of 768 hourly profiles were obtained with the PCADP and ABS, and 385 2-hourly bursts were recorded with the ADVs. Of the PCADP profiles, 401 met the criteria that $r^2 > 0.95$ and $|U| > 0.05$ m/s at ~ 0.35 mab, and 201 of these were associated with ADVF data with noise levels $< 10^{-4}$ m²/s²/Hz. The PCADP velocity profiles showed no systematic deviation from the law of the wall even in the lowest bin that was centered at elevations ranging from 0.07 to 0.2 mab. Tests for curvature in the upper part of the profile (performed by fitting a quadratic, rather than linear, expression in Eq. (6)) indicate that the occurrence of concave and convex profiles is almost evenly distributed and uncorrelated with current speed, acceleration, or wave-orbital velocity.

4.2. Relationship among estimates of shear velocity

The three shear velocity estimates (u_{*EC} from $1/2\text{cov}(\Delta u, \Delta w)$, u_{*LP} from PCADP profiles, and u_{*ID} from vertical spectra at ADVF A) generally agree (within their fairly large ranges of uncertainty) but also exhibit significant scatter (Figs. 5–7, Table 4). The magnitudes correspond closely but, over the 201 measurements, there are significant biases among the three estimates. The median values of u_{*EC} , u_{*LP} , u_{*ID} are 1.0, 1.4, and 1.4 cm/s, respectively. On average, the EC estimates are lower than the others: the median difference $u_{*ID} - u_{*EC}$ is 0.3 cm/s, and the median difference $u_{*LP} - u_{*EC}$ is 0.4 cm/s.

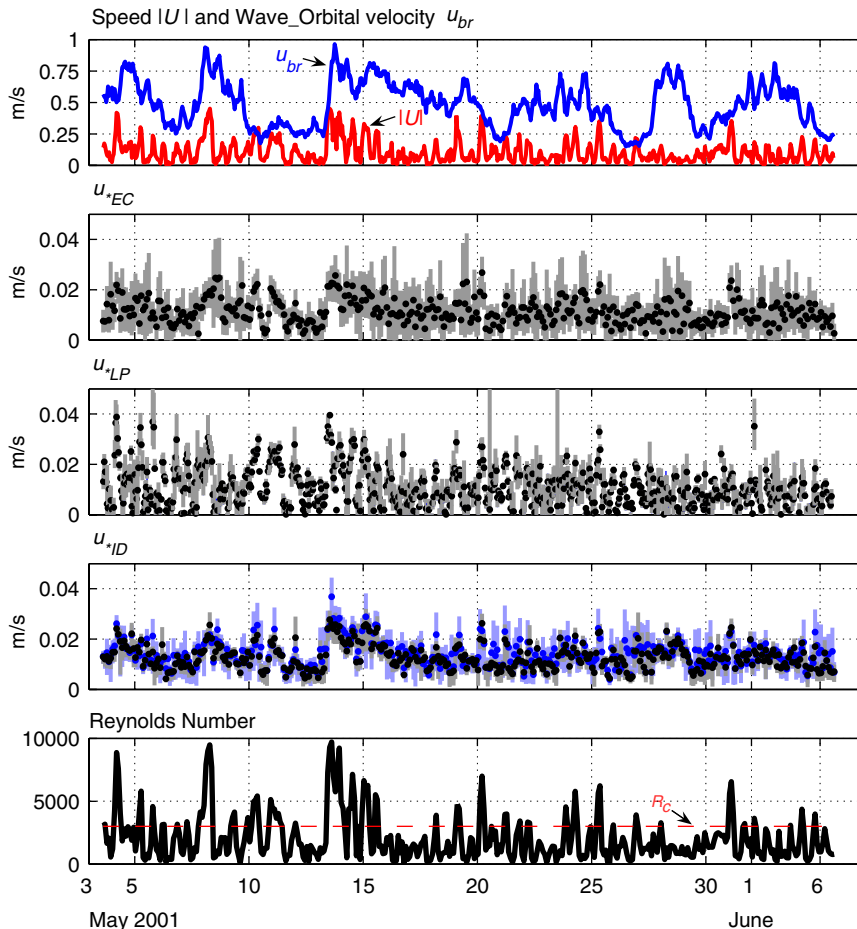


Fig. 5. Measured currents and wave-orbital velocities; shear velocity estimates; and Reynolds number. Shown are (a) mean current speed (red) and wave-orbital velocity (blue); (b) eddy correlation estimates with standard deviations; (c) LP estimates with 90% confidence intervals; (d) inertial dissipation estimates from two instruments (black and blue dots) with 90% confidence intervals (gray and blue bars); and (e) Reynolds number (solid line) based on mean speed and approximate critical value (dashed line).

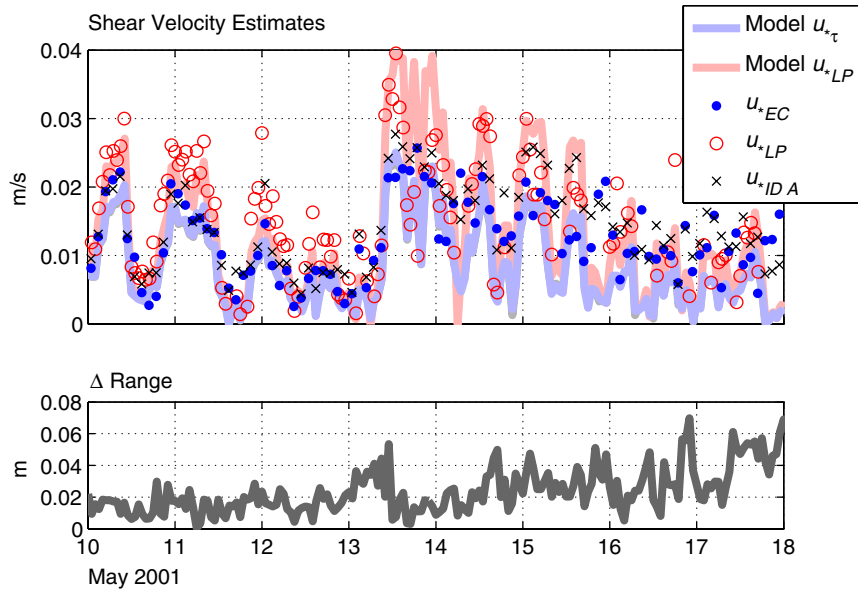


Fig. 6. Expanded time series of (a) estimated shear velocities and (b) difference in range to the bottom among the three PCADP beams (a proxy for bottom roughness). Uncertainty estimates have been omitted for clarity (refer to Fig. 5).

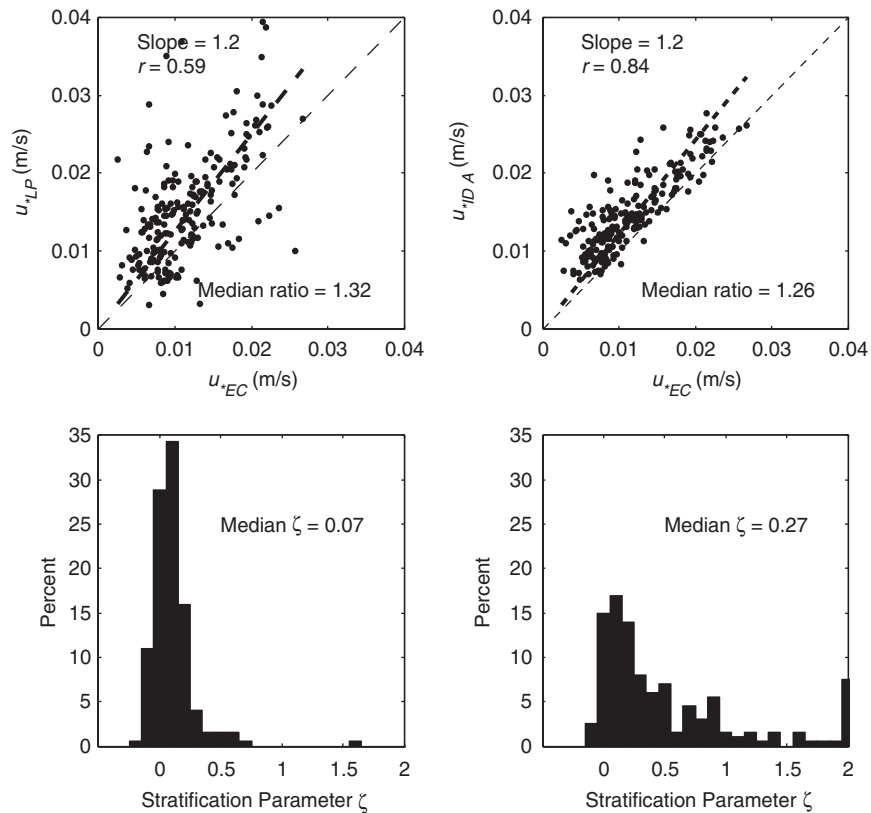


Fig. 7. Scatterplot comparison of the shear-velocity estimates and distributions of stratification parameters estimated from Eqs. (23 and 24).

Table 4

Correlation r among measured and modeled values for the subset ($N = 201$) of 2-hourly samples with speed > 0.05 m/s at ~ 0.35 mab, low noise in the ADVF spectra ($< 10^{-4}$ m²/s²/Hz), and good fits to a log profile ($r^2 > 0.95$)

	$ U $	u	v	u_{br}	Depth	u_{*EC}	$u_{*ID\ A}$	u_{*LP}	$u_{*ID\ B}$	$u_{*\tau\ M}$	$u_{*LP\ M}$	Std(u_*)
$ U $	1	-0.06	-0.09	0.41	0.27	0.82	0.84	0.77	0.74	0.99	0.99	0.21
u	-0.06	1	-0.17	-0.16	0.16	0.00	0.04	-0.14	-0.21	-0.04	-0.08	-0.17
v	-0.09	-0.17	1	0.24	-0.11	-0.07	0.06	-0.02	0.20	-0.16	-0.09	0.04
u_{br}	0.41	-0.16	0.24	1	-0.11	0.37	0.55	0.17	0.49	0.31	0.48	0.16
Depth	0.27	0.16	-0.11	-0.11	1	0.14	0.21	0.27	0.17	0.29	0.24	0.09
u_{*EC}	0.82	0.00	-0.07	0.37	0.14	1	0.84	0.59	0.73	0.82	0.81	-0.01
$u_{*ID\ A}$	0.84	0.04	0.06	0.55	0.21	0.84	1	0.61	0.82	0.82	0.84	0.22
u_{*LP}	0.77	-0.14	-0.02	0.17	0.27	0.59	0.61	1	0.56	0.78	0.74	0.50
$u_{*ID\ B}$	0.74	-0.21	0.20	0.49	0.17	0.73	0.82	0.56	1	0.71	0.74	0.20
$u_{*\tau\ M}$	0.99	-0.04	-0.16	0.31	0.29	0.82	0.82	0.78	0.71	1	0.98	0.20
$u_{*LP\ M}$	0.99	-0.08	-0.09	0.48	0.24	0.81	0.84	0.74	0.74	0.98	1	0.21
Std(u_*)	0.21	-0.17	0.04	0.16	0.09	-0.01	0.22	0.50	0.20	0.20	0.21	1

Uncertainty about the u_{*EC} estimates varies with autocorrelation in the ADVF measurements, and it also increases with wave-orbital velocities. The uncertainties range from 24% to nearly 300%, with a median around 64%. The estimated uncertainties in estimates of u_{*LP} are generally smaller, ranging from 5% to 110% with a median uncertainty of 36%. These are generally higher than uncertainties presented by Lacy et al. (2005), which applied to profiles with $r^2 \geq 0.96$, with velocity measurements at 5 or more points. Uncertainty in the u_{*ID} estimates is larger: $\sim 40\%$ for ADVF A and $\sim 70\%$ for ADVF B. These uncertainties are based on ranges calculated for high and low estimates of dissipation rate (16th and 84th percentile) and maximum and minimum elevations measured by the three PCADP beams.

Fluctuations in the time series of all three u_* estimates (Figs. 5 and 6) are significantly correlated with each other (r ranges from 0.59 to 0.84; Table 4) and with current speed ($r = 0.77$ –0.84). Shear velocities are less well correlated with wave-orbital velocity ($r = 0.17$ –0.55) and these correlations are lowest for u_{*LP} and highest for u_{*ID} . Note also that u_{br} and speed are not independent; they are also correlated ($r = 0.41$) because large waves and wind-driven currents are both associated with storms (Fig. 3). Correlation with scatter among the methods (measured as the standard deviation among the three u_* estimates std(u_*); last column in Table 4) does little to explain the differences among the methods. Std(u_*) is best correlated ($r = 0.5$) with u_{*LP} , merely confirming that u_{*LP} has the most scatter of the three methods.

Expanded time series of the three shear-velocity estimates and results from the one-dimensional wave-current boundary layer model are shown in Fig. 6. The segment shown here includes a representative range of conditions and includes the largest wave events on May 13 and 14. The responses of the shear-velocity estimates during this period were typical of the entire deployment. The upper panel shows agreement among most of the estimates through May 12. During this time, the observational estimates of u_{*LP} were generally higher than the others, and the difference increased with shear velocity. They matched fairly well with model estimates of u_{*LP} . The model estimates of $u_{*\tau}$ tended to be the lowest and generally agreed with observational estimates of u_{*EC} . The dissipation-rate estimates (u_{*IDA}) generally fell between the u_{*LP} and u_{*EC} values. Beginning May 13, the disparity among the three observational estimates increased and after the large wave event, the dissipation-rate estimates (u_{*IDA}) tend to be higher than u_{*EC} and the corresponding model estimate, $u_{*\tau}$.

The lower panel in Fig. 6 shows the maximum difference in transducer elevation among the three PCADP beams (Δr). This provides information about variations of bottom topography over horizontal scales of ~ 0.5 m that may help explain some of the scatter among the time series in the upper panel. In particular, the various estimates diverged early on May 13, at the same time that Δr range was above 0.02 m, and the same phenomenon occurred intermittently for the rest of this interval after the large waves subsided midday on May 14. From midday on May 13–midday on May 14, model

calculations suggest that upper plane bed conditions probably existed, and Δr range was low (Fig. 6(b)). It makes sense that uncertainty in topographic measurements would increase scatter among the u_* estimates because elevation is a factor in the estimates. However, the topographic variations may also indicate bed forms, and wakes shed from these features might affect the boundary layer properties. The model, in particular, includes predictions of bed conditions, and these may differ from actual conditions. We cannot assess this with the present data set, and as there is no systematic relationship between Δr range and $std(u_*)$ that holds for the entire experiment, we can only speculate that elevation uncertainty and bedforms add errors and uncertainty to our modeled and measured estimates of u_* .

The relationships among the three shear velocity estimates over a range of current speeds can be summarized in scatterplots relating u_* to mean

speed (Fig. 8). The thin lines indicate the relationships for two drag coefficients defined in terms of velocity 1 mab (C_{100}). The upper line corresponds to $C_{100} = 7.5 \times 10^{-3}$ ($z_0 = 1$ cm) and the lower line corresponds to the average value of $C_{100} = 3.1 \times 10^{-3}$ ($z_0 = 0.067$ cm) found by Sternberg (1968). These lines help demonstrate that bottom drag tended to decrease with increasing current speed according to all of three of the observational methods and, to a lesser extent, for the model results as well. The exact mechanism for this drag reduction cannot be determined from the measurements, but it appears that any increases in drag caused by enhanced momentum transfer in the wave-boundary and bedload-saltation layers are more than offset by decreases in form drag during upper plane bed conditions and suppression of momentum flux by sediment-induced stratification.

The solid lines in Fig. 8(a–c) connect bin-averaged values for various speed ranges, and the

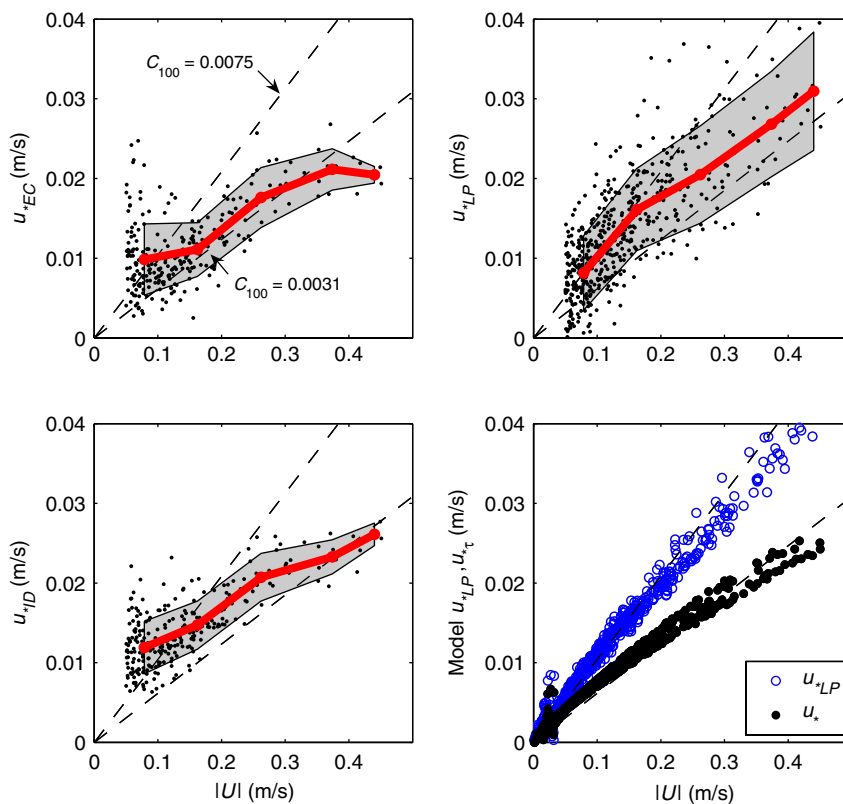


Fig. 8. Scatterplots of shear-velocity estimates as a function of current speed: (a) eddy correlation method, (b) LP method; and (c) inertial dissipation method. In these three panels, the large red dots connected by thick red lines are the mean of all values binned by speed (plotted at the mean speed value) and the gray shading indicates the range between 16th and 84th percentiles. Panel (d) plots estimate u_{*LP} and of $u_{*T} \approx u_{*EC}$ (see text) from the model output. In all panels, lines indicate drag coefficients C_{100} of 7.5×10^{-3} (z_0 of 0.01 m; upper line) and $C_{100} 3.1 \times 10^{-3}$ ($z_0 = 6.7 \times 10^{-4}$ m; lower line; Sternberg, 1968).

gray bands denote the range around each average (16th to the 84th percentiles), quantifying the scatter for each method. The LP method (Fig. 8(b)) has the most scatter, especially at high current speeds. The two other methods have relatively high values of u_* at low current speeds and show a clear decrease in drag at higher current speeds, a result that is inconsistent with Huntley's (1988) correction for low Reynolds numbers. Although it is possible that these correctly reflect increased drag at low speed that is not measured by the log profile method, there are at least two alternative explanations. First, the u_{*EC} and u_{*ID} methods may be increasingly influenced by instrument noise, which would provide an effective lower limit for u_* measurements. Second, as mean current speeds decreased, the number of turbulent vortices advected past our sensors decreased, so the possibility of contamination by wave

motions or advection of wakes from one sensors or tripod legs increased.

4.3. Model results

Results from the one-dimensional model (Figs. 6(a), 8(d), 9, and 10) help in the interpretation of our observations. Typical velocity and concentration profiles from the one-dimensional model are shown in Fig. 9(a) and (b), along with the forcing used in the model (Fig. 9(c)), time series of backscatter profiles obtained with the ABS (Fig. 9(d)) and modeled suspended-sediment concentration (Fig. 9(e)). We have not attempted to calibrate the ABS response beyond the scaling discussed in Section 3.1, or to tune the model to produce accurate suspended-sediment concentrations, but it is clear that sediment resuspension, whether

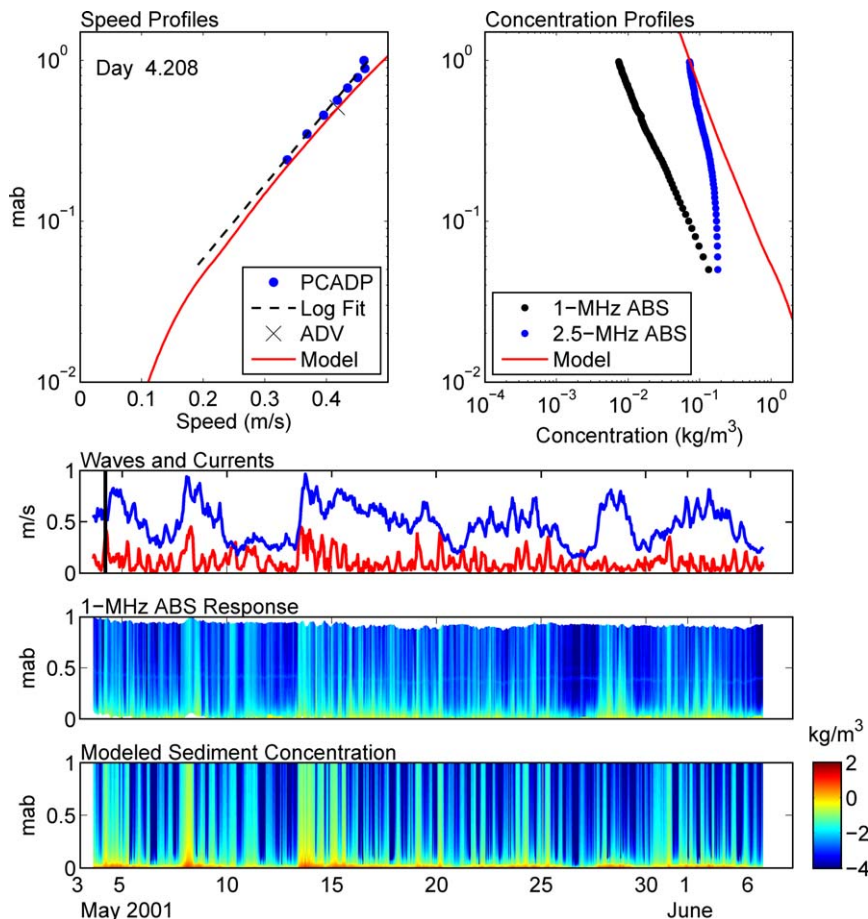


Fig. 9. Typical comparison of model results and observations: (a) Speeds measured by the PCADP (blue dots) and ADV (x), log fit to the PCADP data (dashed line), and modeled results (solid red line); (b) uncalibrated ABS profiles (black and blue dots) and modeled mass concentration profile (red line); (c) wave-orbital velocity and current speed used to force the model (d) profiles of 1-MHz ABS response (arbitrary units, log scale) and (e) profiles of modeled suspended-sediment concentrations (log scale).

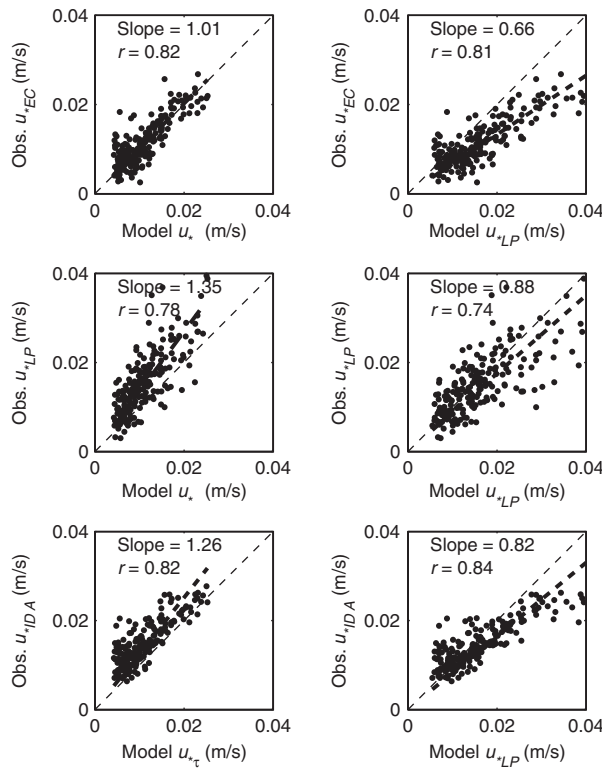


Fig. 10. Scatterplots comparing observed shear-velocity estimates with modeled estimates.

observed or modeled, responded to the local forcing of waves and currents. The contrast between modeled concentration profiles and ABS response in Fig. 9(b) is typical, but the actual variation in profile slopes and magnitudes changed significantly between each hourly observation. We use the ABS data and the modeled suspended-sediment concentrations mostly to support our conclusions that suspended sediment has important effects on our measurements of shear velocity.

Shear velocity estimates obtained by log fits to model velocity profiles (u_{*LP}) are substantially higher than those made from the modeled Reynolds stress at 0.35 mab ($u_{*\tau}$). This is clear in the expanded time series (Fig. 6(a)), the drag-coefficient comparisons (Fig. 8(d)), and scatterplots (Fig. 10), and is consistent with our observations. There is good agreement (slope of the regression fit through zero = 1.01, $r = 0.82$) between modeled $u_{*\tau}$ and observational estimates of u_{*EC} (Fig. 10(a)). Although the agreement is not quite as good (slope = 0.88, $r = 0.74$), the LP estimates from modeled velocity profiles agree best with observational estimates of u_{*LP} (Fig. 10(d)), and the other

comparisons in Fig. 10 show more bias. In the Discussion (Section 5), we argue that the differences between u_* derived from the LP method and u_* derived from modeled Reynolds stresses or estimated from measurements with the EC method can be explained theoretically when stratification is present, but also that the modeled estimate of LP is biased toward higher values.

4.4. Instrument performance

We have tried to ensure that the results are not affected by instrument performance. Careful comparison of the PCADP and ADVFs has been performed by Lacy and Sherwood (2004) and the consistent results, even during times of highest wave-orbital velocities and current speeds, lend confidence to these measurements. Independent measurements of wave and mean-flow statistics at the other tripod locations, including a site ~100 m north of MIA along the 9-m contour, provide no indication that the instruments were grossly in error. Visual inspection and automated editing of the PCADP and ADVF burst measurements suggest these are clean data with relatively few outliers, and the shear velocity estimates produced here are robust regardless of the criteria used to edit the data. The four estimates of u_{*ID} (from horizontal and vertical spectra at the two ADVFs) are well correlated with a slight bias between the horizontal and vertical components and a 10% bias between the two instruments. The very high coherence and almost identical spectral signature of the two ADVFs suggests that the instrumentation for u_{*EC} and u_{*ID} estimates operated correctly (Fig. 4(a,d)).

4.5. Flow disturbance from the tripod

The tripod may have influenced the flow in at least two different ways. First, vortices shed in wakes from the legs and ADVF mounts may have generated small-scale turbulent fluctuations that were not representative of the flow at larger scales. Second, diversion of the flow around the tripod and particularly accelerated flow directed underneath the instrument platform may have impinged on our sample volumes. The effect of vortices shed from tripod legs may be apparent in the directional distribution of turbulence. Shaw et al. (2001) evaluated leg wakes by examining the variance in acceleration of horizontal velocity components A_{vars} .

as a function of mean flow direction. We calculated A_{var} for each burst and looked for directional enhancement of turbulent fluctuations. Turbulence was higher in alongshore directions, but we did not find peaks in turbulent fluctuations aligned with tripod legs. However, wake effects cannot be precluded just because we found no evidence of enhanced turbulence associated with specific mean flow directions; the wave-dominated flow patterns are complex, and the most effective agent for generating and advecting wakes was usually wave-orbital currents.

The larger scale effects of flow deflection around the tripod, or around the package of instrument cases located ~ 1.6 – 2 mab, are difficult to evaluate. Although Lacy and Sherwood (2004) showed that, on average, shear is reduced in the upper part of the PCADP profiles, we could not find evidence for consistent curvature one way or the other in the region immediately above our log fits (i.e., between about 0.5 and 0.8 mab). Flow disturbance in this region is not a source of error to our u_{*EC} estimates, as we did not use it in our log fits. Estimates of u_{*EC} and u_{*ID} might be reduced if distorted streamlines advected turbulence properties from higher elevations to the sensors, but this is only speculation. In summary, we cannot eliminate the possibility that these measurements were influenced by the measurement platform, but neither can we find firm evidence in our data that implicates the tripod.

5. Discussion

5.1. Fundamental differences in u_* estimates

The three methods for estimating u_* are not equally valid estimates of $\sqrt{\tau_b/\rho_0}$. They can be summarized as follows:

$$u_{*EC}^2 = -\overline{u'w'}, \quad (18)$$

$$u_{*LP} = \kappa z \, d|U|/dz, \quad (19)$$

$$u_{*ID} = (\kappa z \epsilon)^{1/3}. \quad (20)$$

The EC estimate (18) provides a direct estimate of the momentum flux towards the seabed and is the most fundamental of the three estimates. If the flow is steady, measurements are accurate, and wave bias is negligible, this method provides estimates of Reynolds stress at the measurement elevation and the only assumption required to relate it to u_* is that the measurements are in the constant stress region.

The LP estimate (19) is a vertically averaged estimate of shear and relies on the law of the wall, an empirical model known to be valid in the constant-stress region of an unstratified boundary layer. The ID method (20) is based on a turbulence model that additionally requires that turbulence production is locally balanced by dissipation. Thus the LP and ID methods are not fundamental estimates of bottom stress because they depend on semi-empirical models that might not be valid for a particular set of measurements.

5.2. Role of stratification

Stratification caused by sediment suspension is a likely reason for failure of the ID and LP methods on the inner shelf. Temperature and salinity gradients are too small to contribute to stratification (Landerman et al., 2004). Stratification introduces another length scale to the problem, and a more complete formulation for shear in a boundary layer is

$$\frac{d|U|}{dz} = \frac{u_*}{\kappa z} (1 + \beta \zeta), \quad (21)$$

where β is a constant (4.7 ± 0.5 ; Businger et al., 1971) and ζ is the dimensionless Monin–Obukhov stability parameter, defined as $\zeta = z/L$ where the Monin–Obukhov length $L = u_*^3/\kappa B$ and buoyancy flux $B = (g/\rho_0)\overline{\rho'w'}$ (e.g., Businger and Arya, 1974; Smith and McLean, 1977; Adams and Weatherly, 1981; Glenn and Grant, 1987; McLean, 1992; Souza and Friedrichs, 2005). In unstratified flows, $\zeta = 0$ and Eq. (19) is recovered and can be integrated to provide the well-known logarithmic boundary layer profile. In stratified flows where $B > 1$ and therefore $\zeta > 1$, the shear increases and the slope $d|U|/dz$ overestimates u_* . We can evaluate the influence of stratification in our measurements by substituting $u_{*LP} = \kappa z \, d|U|/dz$ and $u_{*EC} = u_*$ into Eq. (21) to get

$$\frac{u_{*LP}}{u_{*EC}} = 1 + \beta \zeta. \quad (22)$$

In unstratified flow, the ratio of the two measured values should be unity, and it should be greater than one with stratification. We evaluated this ratio for 201 cases that meet the following criteria: $|U| > 0.05$ m/s, $r^2 > 0.95$ for the log fit, and noise floor $< 10^{-4}$ m²/s²/Hz in the ADVF horizontal spectra. In these cases, u_{*LP} is generally greater than u_{*EC} , but there is substantial scatter (Fig 7(a)).

The slope of the ratio forced through zero is 1.25, with $r = 0.59$, and the median ratio is 1.3. The distribution of ζ calculated from these ratios with Eq. (22) is generally positive and has a median of 0.07 (Fig. 7(c)).

We can also estimate the influence of stratification by examining the budget for turbulent kinetic energy. The TKE budget in steady, uniform flow can be written as

$$-\overline{u'w'} \frac{d|U|}{dz} = \varepsilon - B, \quad (23)$$

where shear production is balanced by dissipation and buoyancy flux and we have assumed that the vertical flux of TKE is negligible, a reasonable assumption near the bed (Tennekes and Lumley, 1972; Pope, 2000). Substituting u_{*EC}^2 for the Reynolds stress, the right side of Eq. (21) for the shear, $\varepsilon = u_{*ID}^3/(\kappa z)$, and $B = u_{*EC}^3 \zeta/(\kappa z)$, the TKE budget (Eq. (23)) can be rewritten as

$$\frac{u_{*ID}^3}{u_{*EC}^3} = 1 + (\beta - 1)\zeta. \quad (24)$$

A comparison of u_{*ID} and u_{*EC} is shown in Fig 7(b). The estimates of u_{*ID} estimates are higher than those of u_{*EC} , and the correlation is better (slope = 1.21, $r = 0.84$, median ratio 1.3) than the correlation of u_{*LP} with u_{*EC} . The corresponding estimates of the stability parameter ζ from Eq. (24) are generally higher (median = 0.27) than those calculated from Eq. (22) and are more broadly skewed toward high values (Fig. 7(d)). The correlation among the two estimates of ζ is weak but significantly different from zero at the 90% confidence level ($r = 0.61$). Somewhat surprisingly, there is no correlation among either estimate of ζ and measures of wave or currents (u_{br} or u_{*EC}). However, the highest values of ζ from Eq. (24) occur when the ratio of waves to currents (u_{br}/u_{*EC}) is highest ($r = 0.80$). This is consistent with the hypothesis that stratification is greatest when waves resuspend sediment but vertical diffusion of the sediment by the mean-flow turbulence is relatively low. A similar relationships hold for ζ based on Eq. (22), but the correlation is lower ($r = 0.47$).

A slightly different method for evaluating the effects of stratification is to estimate the production and dissipation terms in the TKE budget (Eq. (23)) and infer the buoyancy flux from the imbalance. We approximated the Reynolds stresses with $-\overline{u'w'} = u_{*EC}^2$, mean shear with $d|U|/dz = u_{*LP}/\kappa z$, and dissipation with $\varepsilon = u_{*ID}^3/(\kappa z)$. Time series and

histograms of the two terms and their difference (Figs. 11 and 12) show that our estimates of TKE dissipation are slightly higher than our estimates of shear production; the median value of dissipation minus production was 5.4×10^{-6} . The difference in the two, the buoyancy flux B (Figs. 11(b) and 12(c)), is generally positive and moderately well correlated with wave-orbital velocity ($r = 0.50$) but not with current speed ($r = 0.21$; less than the correlation $r = 0.31$ between waves and speed) or water temperature (not significantly different from zero). A quantile–quantile plot (Fig 12(d)), which compares values with the same cumulative probability from two populations, shows that dissipation was higher than production throughout their respective ranges.

We also calculated the time series of buoyancy flux terms from the OBS data in the first part of the deployment before any obvious attenuation by biofouling. Because the OBS respond preferentially to fine material, the concentrations may be overestimated but the gradients may be underestimated. The resulting estimates of suspended-sediment concentrations (not shown) had median values that ranged from 0.1 to 0.8 kg/m^3 at the various elevations, and produced density gradients with median values of $0.2\text{--}0.35 \text{ kg/m}^4$. During the peak of resuspension events, density gradients reached $3\text{--}5 \text{ kg/m}^4$, corresponding to buoyancy production ranging from -10^{-6} to $-10^{-4} \text{ m}^2/\text{s}^3$. Despite the scatter and inherent uncertainty in these calculations, they support the assumption that buoyancy flux associated with sediment-induced stratification is balanced by increased shear and dissipation.

In summary, the results of these analyses strongly implicate sediment-induced stratification as the explanation for biases in estimates of u_{*LP} and u_{*ID} . However, the scatter in these relationships, their small range in parameter space, and the lack of independent estimates of buoyancy flux prevent us from drawing unequivocal conclusions about the role of stratification in this data set.

5.3. Insight from the one-dimensional model

Model calculations typically produce values of u_{*LP} that are higher than values for $u_{*\tau}$ taken at 0.35 mab (as shown in Figs. 6(a) and 10(c,d)). In reality, neither value is necessarily equal to u_{*c} (the current shear velocity that corresponds with time-averaged total bottom stress and sets the scale for eddy viscosity in the model), as illustrated in Fig. 13.

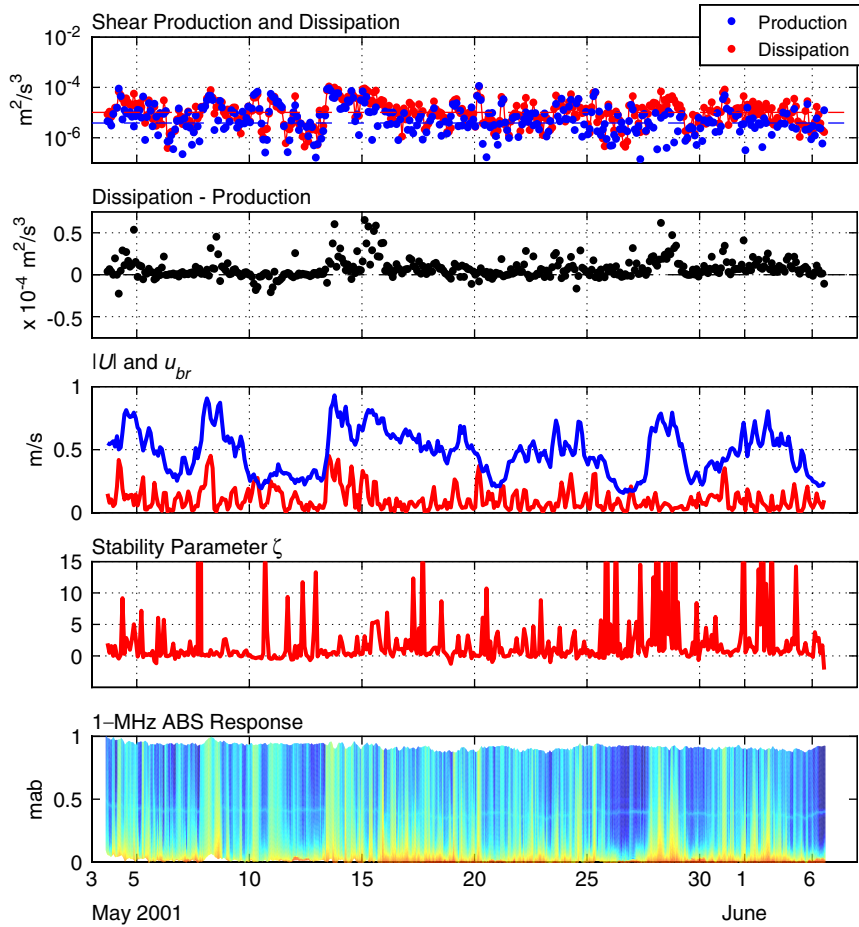


Fig. 11. Time series of (a) TKE production- (blue) and dissipation- (red) rate estimates with lines indicating median values, (b) imbalance in the simple TKE equation (dissipation—production), (c) mean current speed ~ 0.35 mab (red) and wave-orbital velocities (blue), (d) stratification parameter estimated from the imbalance between production and dissipation, and (e) profiles of uncalibrated 1-MHz ABS response.

Under neutrally stratified conditions with no waves (corresponding to black line in Fig. 13), the three values should be very close. The values of u_{*c} and $u_{*\tau}$ match closely in the neutral case, in accord with the model assumption of a constant stress layer, but the value of u_{*LP} is slightly higher because the modeled speed profile is concave downward in the region of the fit (0.2–0.5 mab). The curvature in the neutral case is related to the modeled eddy viscosity high in the profile, which decreases with elevation above the bottom boundary layer. The curvature increases when waves are included, because the model postulates that wave-induced turbulence increases eddy viscosity and decreases shear in lower part of the profile and in the wave boundary layer (blue lines in Fig. 13). The result is that log fits in the region just above the

wave boundary layer tend to overestimate the actual stress at that level in all cases (compare u_{*LP} and $u_{*\tau}$ in Fig. 13). The small differences between u_{*LP} and $u_{*\tau}$ in neutrally stratified conditions arise because the log fits are very sensitive to the shape of the velocity profile, and these differences may be model-specific. Alternative assumptions about the shape of the eddy viscosity profile or a more complicated turbulence submodel might change this result.

The effects of stratification are also elucidated by the one-dimensional model, and these results are more general. When sediment-induced stratification is present, curvature is even more pronounced in the lower portion of the profile (red line in Fig. 13) because the eddy viscosity above the wave boundary layer is reduced by stratification. The relationship

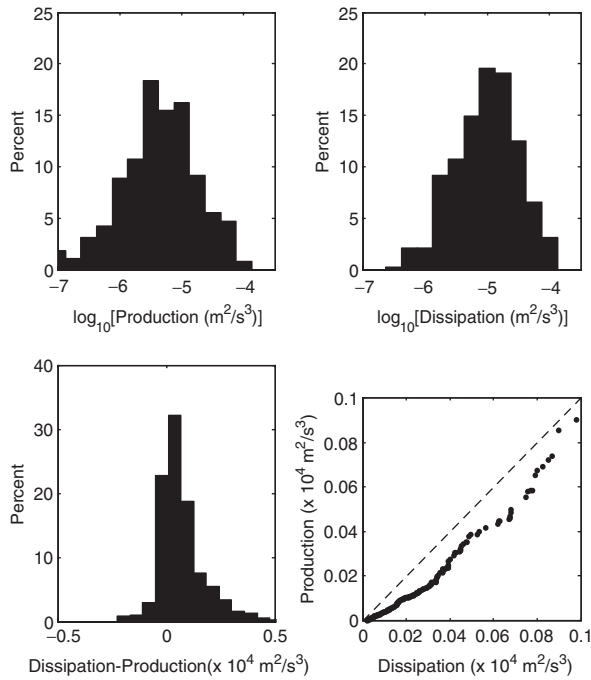


Fig. 12. Comparison of distributions of production and dissipation of TKE estimated from measurements: (a) histogram of production, (b) histogram of dissipation, (c) histogram of dissipation–production, and (d) quantile–quantile plot of dissipation and production.

between $u_{*\tau}$, stress, eddy viscosity and shear is

$$u_{*\tau}^2 = \tau/\rho_0 = -K_m \frac{\partial U}{\partial z} \quad (25)$$

and the stratification correction to K_m causes a reduction that is not completely compensated by increased shear, reducing the modeled Reynolds stress $u_{*\tau}$ at the level of our observations (~ 0.35 mab). This result is not specific to the one-dimensional model we used, and is consistent with the theoretical explanation for why u_{*LP} is high compared with u_{*EC} and u_{*ID} . (e.g., Figs. 5, 6, and 10).

6. Conclusion

Three methods for estimating shear velocity from measurements in a wave-dominated environment have been discussed. These are the EC method, which uses the covariance of the difference in velocity measurements at two adjacent points; the LP method, which uses the slope of velocity profile; and the ID method, which uses the inertial-range spectra of velocity measurements at a single point.

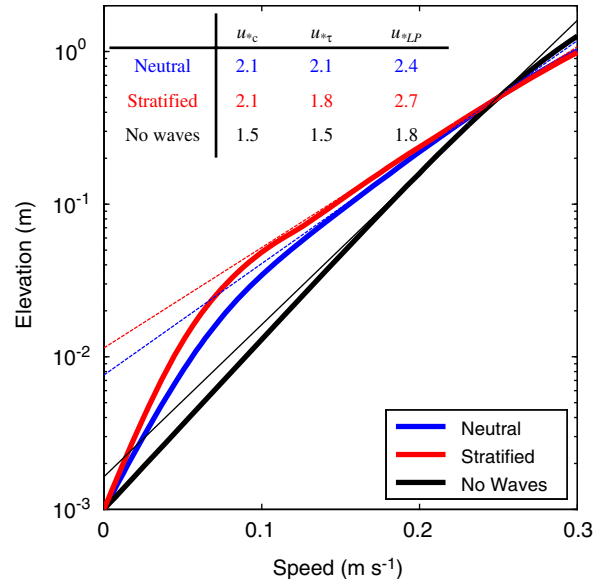


Fig. 13. Velocity profiles (thick lines) from the model with a reference velocity of 0.5 m/s at 0.5 mab, bed sediments (four size classes) similar to the Grays Harbor material, and 10-s waves with orbital velocities u_{br} of 0.4 m/s at 90° to the current direction (except for no wave case, which had $u_{br} = 0$). In the stratified case, the effect of suspended sediment on the eddy viscosity profile was included. Thin lines indicate apparent profiles from logarithmic fits at four elevations matching the PCADP bins. Tabulated values indicate u_{*c} determined by the model, $u_{*\tau}$ calculated from modeled stress at 0.5 mab, and u_{*LP} calculated from the log fits.

All three methods are practical with commercially available instrumentation and the three methods mostly agree (within their broad range of uncertainties) for a month of 2-hourly measurements. The median values for the experiment of u_{*LP} and u_{*ID} were both higher than the median value of u_{*EC} , and pointwise comparisons indicates that $u_{*LP} > u_{*ID} > u_{*EC}$. Boundary-layer theory suggests that of the three methods discussed here, the estimate u_{*EC} is the most fundamental measure of kinematic stress because it is a direct estimate of momentum flux towards the sea bed. It requires only that conditions are fully turbulent, uniform in the along-flow direction, and statistically stationary over a measurement period long enough to measure a representative sample of the velocity field. By comparison, theory indicates that u_{*LP} and u_{*ID} overestimate bottom shear stress when stratification is present, and our data indicate that the effect is important in inner shelf environments when sediment resuspension occurs.

There is significant uncertainty and scatter in our estimates of u_* by all methods. The ranges of

uncertainty are broad, and are themselves uncertain, because the main sources of error in the estimates are violations in the assumptions of stationarity and uniformity, or undersampling of the turbulence field, particularly during times of low mean current speed. The scatter in the measurements is highest for the log profile method, consistent with its sensitivity to stratification. There is also significant scatter and uncertainty in our estimates of stratification parameter. We attribute some of this to changes in bottom topography, and some to the temporal and vertically varying nature of the stratification parameter.

This study provides an important reminder that the traditional LP approach may overestimate shear velocities in shallow, wave-dominated environments. The dissipation-rate method, adjusted for waves according to Trowbridge and Elgar (2001) produced lower values with less scatter that agree more closely with our one-dimensional model, but the EC method of Trowbridge (1998) produced possibly the most accurate, if not the most precise estimates of shear velocity. All of the methods suggest that the drag coefficient decreases with increasing mean current speed and wave-orbital velocity (see also Lacy et al., 2005). Because, in our data set, burst-mean speed and wave-orbital velocity are highly correlated, it is impossible to isolate the cause of this phenomenon. It is clear, however, that the increase in drag caused by enhanced momentum transfer in the wave-boundary and bedload-saltation layers is more than offset by decreases in form drag during upper plane bed conditions and suppression of momentum flux by sediment-induced stratification, in accord with observations by Huntley et al. (1993, 1994). Our qualitative estimates of suspended-sediment concentrations from the ABS and model calculations both implicate sediment-induced stratification as a primary influence in this data set. However, it is appropriate to note that Sternberg's (1968) value of $C_{100} = 3.1 \times 10^{-3}$ always falls within the error bars of at least one of our methods!

Acknowledgments

This study was part of the Southwest Washington Coastal Erosion Study, jointly funded by the US Geological Survey and the Washington State Department of Ecology. We thank Keith Kurrus of Evans-Hamilton Inc., skipper Terry Larson of the *F/V Tricia Rae*, Daryl Slocum and Vadim

Polonichko at Sontek/YSI, George Kaminsky at Ecology, and Guy Gelfenbaum, Dave Gonzales, Kevin O'Toole, Tim Elfers, Jingping Xu, and Joanne Ferriera at the USGS. We also thank investigators at the US Army Corps of Engineers and Pacific International Engineering. Special thanks to Laura Landerman of the USGS, who drafted several of the figures, performed sediment-size analyses, calibrated the OBS, and helped with fieldwork and data analysis. Pat Wiberg generously provided her boundary layer model and Gene Terray, Carl Friedrichs, and Art Trembanis provided insight and suggestions that improved the analyses. Paul Hill, David Huntley, John Warner, and Dave Cacchione made helpful comments on earlier versions of the manuscript. John Trowbridge provided especially valuable comments and suggestions, and motivated much of the analyses presented in the Discussion. Most importantly, CRS would like to thank Dick Sternberg for providing support, formal training, and good advice over the years, and for passing on some of his remarkable intuition for coastal processes. Use of firm and product names is for descriptive purposes only and does not imply endorsement by the US Government.

References

- Adams, C.E., Weatherly, G.L., 1981. Some effects of suspended sediment stratification on an oceanic bottom boundary layer. *Journal of Geophysical Research* 86 (C5), 4161–4172.
- Agrawal, Y.C., Terray, E.A., Donelan, M.A., Hwang, P.A., Williams III, A.J., Drennan, W.M., Kahma, K.K., Kitaigorodskii, S.A., 1992. Enhanced dissipation of kinetic energy beneath surface waves. *Nature* 359, 219–220.
- Bendat, J.S., Piersol, A.G., 1986. *Random Data*, Second ed. Wiley, New York, 566pp.
- Bowden, K.F., 1962. Turbulence. In: Hill, M.N. (Ed.), *The Sea*, Vol. 1. Wiley-Interscience, New York, pp. 802–825.
- Bryan, K.R., Black, K.P., Gorman, R.M., 2003. Spectral estimates of dissipation rate within and near the surf zone. *Journal of Physical Oceanography* 33 (5), 979–993.
- Businger, J.A., Arya, S.P.S., 1974. Height of the mixed layer in the stably stratified planetary boundary layer. In: Frenkiel, F.N., Munn, R.E. (Eds.), *Advances in Geophysics*, 18A. Academic Press, New York, pp. 73–92.
- Businger, J.A., Wyngaard, J.C., Izumi, Y., Bradley, E.F., 1971. Flux profile relationships in the atmospheric surface layer. *Journal of Atmospheric Science* 28, 190–201.
- Cacchione, D.A., Drake, D.E., 1990. Shelf sediment transport: an overview with applications to the northern California continental Shelf. In: LeMehaute, B., Hanes, D.M. (Eds.), *The Sea*, 9, Part B. Wiley Interscience, New York, pp. 729–773.
- Champagne, F.H., Friehe, C.A., LaRue, J.C., Wyngaard, J.C., 1977. Flux measurements, flux estimation techniques and

- fine-scale turbulence measurements in the unstable surface layer over land. *Journal of Atmospheric Science* 34, 515–530.
- Cheng, R.T., Ling, C.-H., Gartner, J.W., 1999. Estimates of bottom roughness length and bottom stress in South San Francisco Bay, California. *Journal of Geophysical Research* 104 (C4), 7715–7728.
- Deacon, E.L., 1959. The measurement of turbulent transfer in the lower atmosphere. *Advances in Geophysics* 6, 211–228.
- Gibbs, R.J., Matthews, M.D., Link, D.A., 1971. The relationship between sphere size and settling velocity. *Journal of Sedimentary Petrology* 41 (1), 7–18.
- Glenn, S.M., Grant, W.D., 1987. A suspended sediment stratification correction for combined wave and current flows. *Journal of Geophysical Research* 92 (C8), 8242–8264.
- Grant, W.D., Madsen, O.S., 1986. The continental shelf bottom boundary layer. *Annual Review of Fluid Mechanics* 18, 265–305.
- Grant, W.D., Williams III, A.J., Glenn, S.M., 1984. Bottom stress estimates and their prediction on the northern California continental shelf during CODE-1: the importance of wave-current interaction. *Journal of Physical Oceanography* 14, 506–527.
- Green, M.O., 1992. Spectral estimates of bed shear stress at subcritical Reynolds numbers in a tidal boundary layer. *Journal of Physical Oceanography* 22, 903–917.
- Gross, T.F., Nowell, A.R.M., 1983. Mean flow and turbulence scaling in a tidal boundary layer. *Continental Shelf Research* 2, 109–126.
- Gross, T.F., Isley, A.E., Sherwood, C.R., 1992. Effective roughness changes during storms on the Northern California shelf. *Continental Shelf Research* 12 (2/3), 389–414.
- Gross, T.F., Williams, A.J., Terray, E.A., 1994. Bottom boundary layer spectral dissipation estimates in the presence of wave motions. *Continental Shelf Research* 14 (10/11), 1239–1256.
- Heathershaw, A.D., Simpson, J.H., 1978. The sampling variability of the Reynolds stress and its relation to boundary stress and drag coefficient measurements. *Estuarine and Coastal Marine Science* 6, 263–274.
- Huntley, D.A., 1988. A modified inertial dissipation method for estimating seabed stresses at low Reynolds numbers, with application to wave/current boundary layer measurements. *Journal of Physical Oceanography* 18, 339–346.
- Huntley, D.A., Hazen, D.G., 1988. Seabed stresses in combined wave and steady flow conditions on the Nova Scotia Continental Shelf: field measurements and perdutions. *Journal of Physical Oceanography* 18, 347–362.
- Huntley, D.A., Huthnance, J.M., Collins, M.B., Liu, C.-L., Nicholls, R.J., Hewitson, C., Green, M.O., Dyer, K.R., Jago, C.F., 1993. Hydrodynamics and sediment dynamics of North Sea sand waves and sand banks (and Discussion). *Philosophical Transactions of the Royal Society of London A* 343, 461–474.
- Huntley, D.A., Nicholls, R.J., Liu, C.-L., Dyer, K.R., 1994. Measurements of the semi-diurnal drag coefficient over sand waves. *Continental Shelf Research* 14 (5), 437–456.
- Komar, P.D., 1998. *Beach Processes and Sedimentation*, Second ed. Prentice-Hall, New Jersey, 544pp.
- Kim, S.-C., Friedrichs, C.T., Maa, J.P.-Y., Wright, L.D., 2000. Estimating bottom stress in tidal boundary layer from acoustic Doppler velocimeter data. *Journal of Hydraulic Engineering* 126 (6), 399–406.
- Lacy, J.R., Sherwood, C.R., 2004. Accuracy of a pulse-coherent acoustic Doppler profiler in a wave-dominated flow. *Journal of Atmospheric and Oceanic Technology* 21, 1448–1461.
- Lacy, J.R., Sherwood, C.R., Wilson, D.J., Chisholm, T.A., Gelfenbaum, G.R., 2005. Estimating hydrodynamic roughness in a wave-dominated environment with a high resolution acoustic Doppler profiler. *Journal of Geophysical Research* 110, C06014.
- Landerman, L.A., Sherwood, C.R., Gelfenbaum, G., Lacy, J., Ruggiero, P., Wilson, D., Chisholm, T., Kurrus, K., 2004. Grays Harbor Sediment Transport Experiment Spring 2001: Data Report. US Geological Survey Data Series DS-98, Menlo Park, CA.
- Large, W.G., Pond, S., 1981. Open ocean momentum flux measurements in moderate to strong winds. *Journal of Physical Oceanography* 11, 324–336.
- Long, C.E., Wiberg, P.L., Nowell, A.R.M., 1993. Evaluation of von Karman's constant from integral flow parameters. *Journal of Hydraulic Engineering* 119 (10), 1182–1190.
- Lueck, R.G., Wolk, F., 1999. An efficient method for determining the significance of covariance estimates. *Journal of Atmospheric and Oceanic Technology* 16, 773–775.
- Lumley, J.L., Terray, E.A., 1983. Kinematics of turbulence convected by a random wave field. *Journal of Physical Oceanography* 13, 2000–2007.
- Madsen, O.S., 1994. Spectral wave-current bottom boundary layer flows. *Coastal Engineering 1994*. Proceedings, 24th International Conference Coastal Engineering Research Council, 384–398.
- McLean, S.R., 1992. On the calculation of suspended load for noncohesive sediments. *Journal of Geophysical Research* 97 (C4), 5759–5770.
- Pope, S.B., 2000. *Turbulent Flows*. Cambridge University Press, Cambridge, 771pp.
- Shaw, W.J., Trowbridge, J.H., 2001. The direct estimate of near-bottom turbulent fluxes in the presence of energetic wave motions. *Journal of Atmospheric and Oceanic Technology* 18, 1540–1557.
- Shaw, W.J., Trowbridge, J.H., Williams III, A.J., 2001. Budgets of turbulent kinetic energy and scalar variance in the continental shelf bottom boundary layer. *Journal of Geophysical Research* 106 (C5), 9551–9564.
- Smith, J.D., McLean, S.R., 1977. Spatially averaged flow over a wavy surface. *Journal of Geophysical Research* 82 (12), 1735–1746.
- Soulsby, R.L., 1980. Selecting record length and digitization rate for near-bed turbulence measurements. *Journal of Physical Oceanography* 10, 208–219.
- Souza, A., Friedrichs, C., 2005. Near-bottom boundary layers. In: Baumert, H., Simpson, J.D., Sündermann, J. (Eds.), *Marine Turbulence: Theories, Observations, and Models*. Cambridge University Press, Cambridge, pp. 283–296.
- Sternberg, R.W., 1968. Friction factors in tidal channels with differing bed roughness. *Marine Geology* 6, 243–260.
- Taylor, G.I., 1938. The spectrum of turbulence. *Proceedings of the Royal Society of London, Series A* 164, 476.
- Tennekes, H., Lumley, J.L., 1972. *A First Course in Turbulence*. The MIT Press, Cambridge, MA, p. 300.
- Traykovski, P., Wiberg, P.L., Geyer, W.R., 2005. Observations and modeling of wave-supported sediment gravity flows on the Po prodelta and comparison to prior observations from the Eel shelf. *Continental Shelf Research*, in press.

- Trowbridge, J.H., 1998. On a technique for measurement of turbulent shear stress in the presence of surface waves. *Journal of Atmospheric and Oceanic Technology* 15, 290–298.
- Trowbridge, J., Elgar, S., 2001. Turbulence measurements in the surf zone. *Journal of Physical Oceanography* 31, 2403–2417.
- Voulgaris, G., Trowbridge, J.H., Shaw, W.J., Williams III, A.J., 1997. High resolution measurements of turbulent fluxes and dissipation rates in the benthic boundary layer. *Coastal Dynamics '97. Proceedings of the Conference of American Society of Civil Engineers*, 177–186.
- Wiberg, P.L., Harris, C.K., 1994. Ripple geometry in wave-dominated environments. *Journal of Geophysical Research* 99 (C1), 775–789.
- Wiberg, P.L., Rubin, D.M., 1989. Bed roughness produced by saltating sediment. *Journal of Geophysical Research* 94 (C4), 5011–5016.
- Wiberg, P.L., Smith, J.D., 1983. A comparison of field data and theoretical models for wave–current interaction at the bed on the continental shelf. *Continental Shelf Research* 2, 147–162.
- Wiberg, P.L., Drake, D.E., Cacchione, D.A., 1994. Sediment resuspension and bed armoring during high bottom stress events on the northern California inner continental shelf: measurements and predictions. *Continental Shelf Research* 14 (10/11), 1191–1219.
- Xu, J.P., Wright, L.D., Boon, J.D., 1994. Estimation of bottom stress and roughness in Lower Chesapeake Bay by the inertial dissipation method. *Journal of Coastal Research* 10 (2), 329–338.